Experimental Evaluation of the Aerodynamic Rotor/Propeller Interactions on High Speed Helicopters, Efforts and Velocity Fields Measurements

Lauriane Lefevre, Vianney Nowinski, Jérôme Delva, Antoine Dazin

Experimental Evaluation of the Aerodynamic Rotor/Propeller Interactions on High Speed Helicopters, Efforts and Velocity Fields Measurements

Lauriane Lefevre [a]	**Vianney Nowinski** [a]	**Jérôme Delva** [a]	**Antoine Dazin** [a]
Ph. D Candidate	Doctor		Professor
ONERA	ONERA	ONERA	ENSAM
Lille, France	Lille, France	Lille, France	Lille, France

(a) Univ. Lille, CNRS, ONERA, Arts et Métiers Institute of Technology, Centrale Lille, UMR 9014-LMFL-Laboratoire de Mécanique des Fluides de Lille - Kampé de Fériet, F-59000, Lille, France.

ABSTRACT

This paper focuses on the experimental evaluation of the rotor/propeller interactions for hybrid compound configurations. Experiments are conducted in the ONERA L2 large size-low speed wind tunnel with a 1/7.7 Dauphin 365N model and a four-bladed small-scale propeller. Measurements are realized using two six-component balances, accelerometers, and blade pitch, flap and lead-lag angle sensors. PIV measurements are performed to visualize the velocity fields around the helicopter. Different flight conditions (wind speeds and propeller rotational speeds) have been tested. The comparison of the results obtained with an isolated main rotor and an isolated propeller with the complete assembly highlighted the influence of their interactions on their performances. In hover, the propeller is completely immersed in the rotor wake, and the thrust is therefore maximal. At low speed, the propeller is partially immersed and the flow on the propeller disk is highly asymmetrical. No direct interactions are measured at high speed, where the interactions increase the performances of the propeller due to the increased angle of attack of the flow on the propeller disk.

NOTATION

b	Number of rotor blades
c	Blade chord (m)
Fz	Thrust (N)
R_{prop}	Propeller radius (m)
R_{rotor}	Rotor radius (m)
S	Rotor disk surface (m²)
V	Free stream velocity (m/s)
V_{tip}	Blade tip rotation velocity (m/s)
$\bar{Z}$	Thrust coefficient ($\bar{Z} = \frac{100.Fz}{\frac{1}{2}\rho S\sigma(R\Omega)^2}$)
α	Flow angle (α = arctan(V / U), °)
μ	Advance ratio (μ = V/V_{tip})
ρ	Air density (kg/m^3)
σ	Rotor solidity ($\sigma = \frac{b\,c}{\pi\,R_{rotor}}$)
Ω_{prop}	Propeller rotational velocity (rpm)
Ω_{rotor}	Rotor rotational velocity (rpm)

INTRODUCTION [1]

Helicopters are widely recognized for their hovering and vertical take-off and landing (VTOL) capabilities. While the demand has increased due to the multiplication of air transport, classical configurations present limitations: 1) a maximum speed limited to around 300 km/h, 2) a low load capacity, 3) a small autonomy, and 4) a questionable comfort due to vibrations and noise.

To increase the maximal reachable speed, the compound helicopters have been created. Including additional lift wings and/or rotor, these setups beget a rotor slow-down allowing the device to reach higher speeds without undergoing compressibility issues taking place on the advancing side of the main rotor on conventional gyrodines. Amongst the compound configurations, the hybrid helicopter is equipped with two side propellers assembled on a lift-wing. Two examples are the Eurocopter X3 that reached the velocity of 472 km/h in 2014, and the Airbus Helicopters RACER that is expected to have a cruise speed of 400km/h (Figure 1). In this configuration, the

propellers have two key functions: 1) providing thrust to increase the maximum speed, and 2) creating an efficient anti-torque to preserve the hovering abilities.

Figure 1 - Eurocopter X3 (left) and Airbus Helicopters RACER (right)

However, this configuration undergoes complex and important interactions between rotating elements. Numerical studies have been conducted on the rotor/wing (Ref. 1, Ref. 2, Ref. 3, Ref. 4, Ref. 5), rotor/fuselage (Ref. 6, Ref. 7), wing/propeller (Ref. 8), and rotor/propeller interactions (Ref. 9), but very few experimental research is available to date (Ref. 10, Ref. 11). In this context, this paper presents the experimental characterization of the aerodynamic rotor/propeller interactions on an hybrid compound helicopter for different flight configurations.

The objective of this study is to estimate the influence of the interactions on the performances of the rotating elements.

To do so, efforts and velocity fields measurements are conducted. Experiments took place in the ONERA L2 large size-low speed wind tunnel with a small-scale DAUPHIN 365N model and a four-bladed propeller.

This paper analyzes efforts measurements for advance ratios up to 0.22. Velocity fields measurements at low (μ = 0.06) and high speeds (μ = 0.22) are also examined. Then, the influence of the advance ratio on the rotor/propeller interactions is presented. For each flight configuration, the influence of the interactions on the rotating elements performances is discussed.

EXPERIMENTAL SETUP

The main rotor

A 1/7.7 scale DAUPHIN 365N helicopter has been used for this study (Figure 2). This glass fiber model has been studied at ONERA since its manufacturing in the 1980's (Ref. 12, Ref.13). The model is 1.467 m long and 0.417 m high. The rotor is fully articulated and equipped with four rectangular blades with the following characteristics: blade section OA209, a chord of 0.05 m, linear twist angle of -16 °/m, made of glass-filled nylon. The rotor diameter is 1.5 m and the head is tilted 4° towards the nose of the device.

The thrust coefficient is preserved compared to the full-scale helicopter ($\overline{\boldsymbol{Z}}$ = 14.5 to represent a moderate loading). The nominal rotational speed is 1100 rpm, which corresponds to a blade tip speed of 86 m/s. The measurement uncertainty is less than 50 rpm at the nominal rotational speed. The advancing side of the rotor is on the port side, over the propeller.

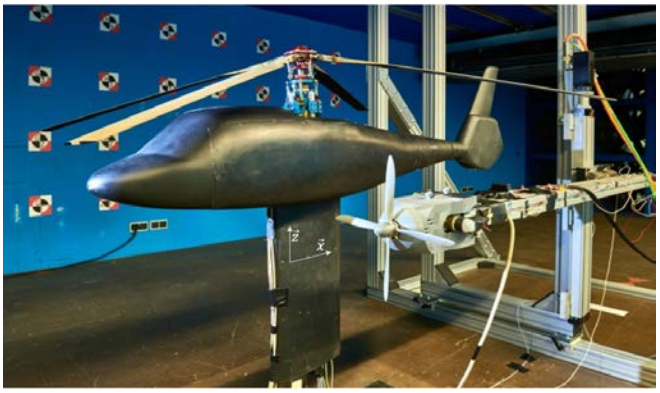

Figure 2 - Installation of the full assembly in the L2 wind tunnel

The loads are measured using a 6-axis aerodynamic balance placed under the model, and accelerometers are set in two directions. The balance is custom made, and has been designed to have a measurement uncertainty of less than 1 %.

As for a full-size helicopter, the collective and cyclic pitch angles are controllable and measurable. The blade pitch, flap and lead-lag angles are also monitored. An air-cooling circuit is installed to limit the motor heating during the measurements. The loads created by the pressure are considered negligible. Measurements are monitored via LabVIEW, also used to set the rotational speeds of the rotors. The analysis is performed using a python code. The efforts coordinate system is defined such that $\vec{\boldsymbol{x}}$ is directed towards the tail of the helicopter, $\vec{\boldsymbol{y}}$ towards starboard and $\vec{\boldsymbol{z}}$ towards the ceiling. Important resonance effects have been measured on the helicopter. To ensure the safety of the device, the rotational speed of the main rotor has been chosen to avoid the resonance frequencies.

The side propeller

The propeller (Figure 3) has been chosen to mimic the Eurocopter X3 dimensions, thrust, and tip speed. A four-blade off-the-shelf propeller supplied by APC Propeller has been used. The propeller is made of glass-filled nylon. A diameter of 0.28 m (11 inches) has been chosen to keep the geometric propeller to main rotor diameter ratios between the model and the real configuration. The blade twist is 9°. The geometry of the blade has been provided by the supplier, and the 2D airfoil tables have been obtained using the elsA CFD software (Ref. 14).

Measurements are performed with an AMTI MC3A six-axis balance. It has a non-linearity of ±0.2 % at full scale

and a transverse sensibility lower than 2 %. The balance has been calibrated to have a full scale of Fz = 94 N. The balance is connected to a GEN5 conditioner. The assembly is also equipped with a resistance thermometer (PT100). A temperature divergence has been identified on the propeller balance during the preparatory work. This divergence has been corrected with experimentally determined linear parameters. The efficiency of the correction has been proven.

To obtain a smoother flow, a tip cone has been set. In addition, a fairing has been created to isolate the balance from the flow created by the propeller wake and the wind. A preliminary study proved the efficiency of these devices which are kept for the entire study on the complete assembly.

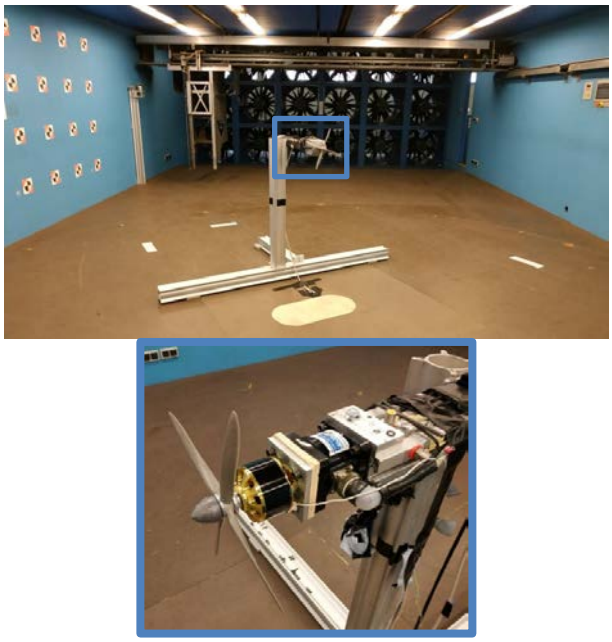

Figure 3 - Isolated small-scale propeller mounted in the L2 subsonic wind tunnel

For each operating point, averaged values of the efforts have been evaluated among 90 000 consecutives measurements. The 95 % confidence interval plotted in red in the loads figures show the good quality of the averages values presented in the paper.

Strong resonance effects have been identified on the propeller during the preliminary study. To limit the influence on the results, a sixth order low-pass filter has been applied at 150 Hz on the propeller balance measurements to limit the influence of the vibrations on the measures.

L2 wind tunnel

This study has been conducted in the ONERA large size-low speed L2 wind tunnel (Figure 4). This facility is in operation since 1968 for naval, industrial, and aeronautical applications with a broad panel of measurement techniques. The test section is 6 x 2.4 x 13 m^3.

To adjust the assembly position, a rotating plate with a 5.96 m diameter is integrated in the wind tunnel floor. The measured drift angle is set with an uncertainty of less than 0.1°. The center of the rotating disk is located in the middle of the test section, 6.5 m downstream of the honeycomb. In this study, the side-slip angle of the structure has not been modified since the propeller's structure is not centered on the rotating disk.

The air circulation is carried out by eighteen fans divided into three horizontal lines and six columns. All together, the fans power is 125 kW, and they can generate a maximum velocity of 19 m/s in the test section. The flow is then delivered to the rear part of the hall where it freely diffuses to the sides and top before returning to the entrance of the tunnel at a low velocity. Before reentering the test section, the air goes through a honeycomb to limit turbulence and to align the flow in the axial direction. The wind tunnel operates at ambient atmospheric conditions. The humidity, the ambient static pressure, and temperature are measured in the undisturbed air in the hall. Considering the low velocities involved, the natural heat transfers only generates a 5°C per hour temperature increase in continuous operations at full power thanks to the air flow stream that ensures the cooling of the fans electric engines. A maximal air density variation of 2 % has been observed during the test, which is why no correction has been applied. Moreover, Pitot tubes are implemented in the vein to monitor the evolution of the real wind speed during the tests.

The turbulence profile shows values up to 7.6 % close to the walls, and less than 3 % in the middle of the section. These values depend on the wind speed and the geometry of the tested bench. In this study, it has been proven that the blockage effect due to the test bench is small as the propeller disk only covers 0.43 % of the wind tunnel test section.

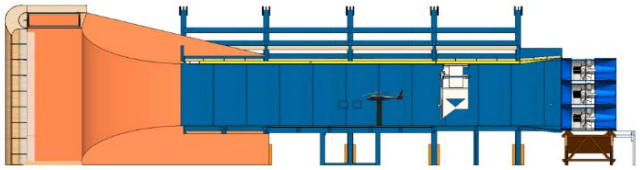

Figure 4 - Scheme of the INTROH bench mounted in the L2 subsonic wind tunnel

SPIV setup

Stereoscopic PIV measurements have been conducted for several flight configurations. The air has been seeded with fine droplets of olive oil. With a density of 0.9137 g/cm^3, the fluid has proven its ability to not disrupt the natural air flow while effectively reflecting light. The pot used for this campaign produces droplets with a diameter of 10 µm, and is placed approximatively two meters upstream

to the honeycomb to ensure the homogeneity of the seeding in the test section.

The acquisition plane is placed upstream to the propeller. The PIV plane measures 325 mm x 340 mm. The tip of the propeller cone is located at (150 mm, -120 mm), and the tip of the propeller blade is located just over the point of maximum velocity (y = 20 mm). The Figure 5 suggests that the main rotor interfere in the measurement window, but the rotation leads to an elevation of the blades. Therefore no interference between the measurement window and the PIV plane is observed during the tests. The plane has a resolution of one vector every 3 mm to 6 mm.

The PIV coordinate system is defined such that $\vec{x}$ is directed towards the tail of the helicopter, and $\vec{y}$ towards the ceiling. The out of-plane velocity is positive when the particules evolve towards the left side of the helicopter from the pilot's point of view.

For all the velocity fields presented in this article, U is the velocity along $\vec{x}$ and directed towards the tail of the aircraft, V is the vertical velocity directed towards the rotor head, and W the out of-plane component defined such that a positive velocity is directed towards the rotor blades tip. The in-plane norm of the velocity is calculated with $\boldsymbol{Norm} = \sqrt{\boldsymbol{U}^2 + \boldsymbol{V}^2}$.

Figure 5 - Scheme of the PIV plane placement on the full assembly

The image acquisition is performed with a laser and two high resolution cameras. The 2 x 400 mJ pulsed laser is activated at a wave length of 532 nm. The acquisition frequency is of 5 Hz, which allows the decoupling the PIV results with the rotor frequency (16.7 Hz) and to focus on the analysis on the rotor wake rather than blade passing unsteady effects. The pulse duration is of 5 ns.

The LaVision 4M cameras have a resolution of 2048 x 2048 pixels. The square pixels measure 7.4 µm x 7.4 µm. Particles therefore extend over 1.5 pixels. The time step is chosen for each wind speed to allow a typical particles displacement of 5 to 6 pixels between the two images. The spatial resolution of the interrogation windows is of 4.7 mm to 4.9 mm depending on the flight configuration. An overlapping of 70% of the interrogation windows is set. The cameras are positioned at a lateral distance of 2.1 m on the port side of the helicopter. The first camera is positioned at ground level, while the second is placed at 2.055 m height (Figure 6). The cameras cover an angle of about 50°, which allows the determination of the three components of the velocity.

Figure 6 - Implementation of the PIV setup in the L2 wind tunnel during calibration

The ONERA FOLKI software (Ref. 15) is used to reconstruct the velocity fields based on a modified iterative wrapping similar to the dense Lukas-Kanade algorithm (Ref. 16). The window size is of 32 x 32 pixels², which gives a good compromise between the visualization of the local phenomenon and a good correlation. With this tool, the overall uncertainty of the velocity profiles calculated with the Wieneke method is under 5 % on at least 80 % of the PIV plane.

Tests conducted

A parametric study has been conducted to analyze the influence of the flight conditions on the performances of the aircraft. During the campaign, the wind speed varies from 0 m/s to 19 m/s, operating through all the L2 wind tunnel capabilities. Considering the rotational speed of the main rotor, this corresponds to advance ratios from µ = 0.00 to µ = 0.22.

During the efforts measurements, the other parameter studied is the propeller rotational speed varying from 0 rpm to 9500 rpm. Ω_{prop} is set with an accuracy of ±30 rpm, and measured with an uncertainty of less than 1 %. For each test, the data is recorded at 3000 Hz during 30 seconds.

Velocity fields measurements were also realized for advance ratios ranging from 0.00 to 0.22. All the PIV measurements presented in this article are performed at Ω_{rotor} = 1100 $\pm\mathbf{10}$ rpm and Ω_{prop} = 7500 $\pm\mathbf{30}$ rpm. The data are recorded for 10 minutes, allowing 3000 frames per

flight case to be extracted. Unless otherwise noted, the set of velocity field images presented in this paper are average fields over the complete set. Averages are calculated by considering only the points with a cross correlation greater than 0.2, meaning that at least 20% of the particle are observed in both images.

During the entire campaign, three trim conditions are set : the thrust ($\mathbf{F_{z,rotor}}$) is of 99.3 N, which corresponds to a thrust coefficient $\bar{\mathbf{Z}} = \mathbf{14.5}$. The thrust is set with an uncertainty of ± 3 N. The longitudinal load ($\mathbf{F_{x,rotor}}$) is adjusted to compensate the fuselage drag previously identified on the isolated helicopter, with an accuracy of ± 0.5 N. To suppress the lateral effort ($\mathbf{F_{y,rotor}}$), the longitudinal flap angle ($\boldsymbol{\beta_{1s}}$) is zero [±0.5°]. In all the loads figures presented, the 95 % confidence interval is plotted in red.

For all the tests presented in this article, the propeller is placed below the main rotor advancing blade, on the port side of the helicopter. The studied position is similar to what can be observed on the Eurocopter X3: The propeller is placed 0.14 m ahead of the rotor center (one propeller radius), at half a rotor radius laterally (0.375 m), and 0.28 m under the rotor head.

RESULTS

Isolated Main Rotor

A preparatory study has been conducted with HOST (Helicopter Overall Simulation Tool, Ref. 17), a helicopter simulation software used amongst others to perform trim calculation or rotor flight loads estimations. In this study, HOST has been used to predict the commands to impose to reach the objective trim. The numerical predictions are close to the experimental measurements observed as the relative differences are less than 5% (Figure 7).

The differences observed between the numerical and the experimental approaches are explained by 1) the modification of the rotating speed of the main rotor, and 2) an offset created when calibrating the sensors of the model. The offset has been kept for the entire campaign to allow the main rotor to reach the thrust objective set.

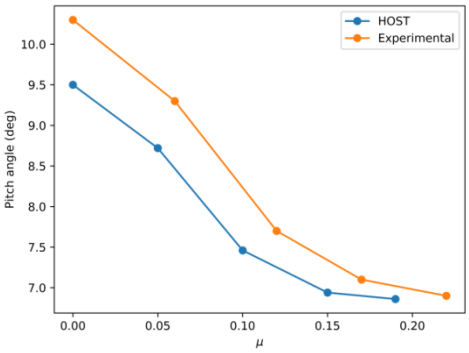

Figure 7 - Experimental and numerical pitch angle of the isolated main rotor depending on the advance ratio

The longitudinal efforts are also observed to determine the fuselage drag depending on the advance ratio (Figure 8). The drag is compensated when piloting the helicopter during the rest of the study.

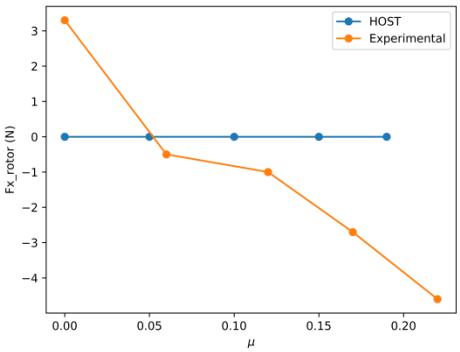

Figure 8 – Experimental and numerical longitudinal effort on the isolated main rotor depending on the advance ratio

Isolated Propeller

The first step of this experimental study consisted in the characterization of the isolated propeller for different flight scenarios (Ref. 18). The experimental characterization of the isolated propeller depending on the side slip angle shows that the resulting thrust is increased by 3 % when the propeller is placed at 90° (Figure 9). This is due to the increased angle of attack on the propeller blades.

Considering that the measures at Ω_{prop}= 0 rpm are the same for all the side slip angles, the wall and blockage effects are considered negligible. This is a consequence of the small dimensions of the propeller (R = 0.14 m) compared to the wind tunnel test section.

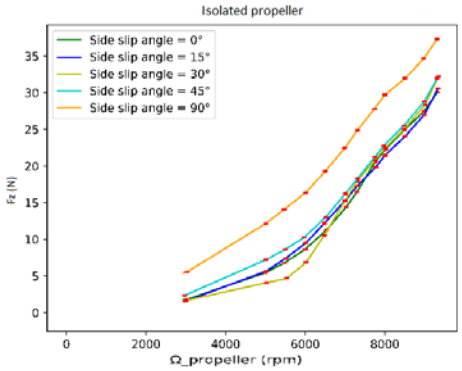

Figure 9 - Influence of the sideslip angle on the thrust of the isolated propeller

The study on the isolated propeller highlighted the loss of thrust as a result of increasing wind speed due to the increase of the angle of attack of the flow on the propeller disk (Figure 10).

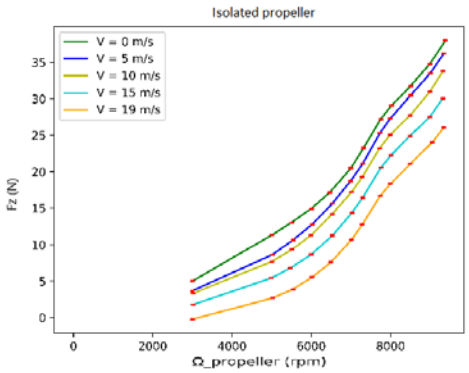

Figure 10 - Thrust of the isolated propeller for different advance ratio

This preliminary study allowed the determination of the efforts on the isolated propeller, and will be used as the reference to evaluate the influence of the rotor wake. Complementary tests higlighted the absence of stall for all flight conditions.

Interactions in Hover

This section presents an investigation of the rotor/propeller interactions for flights at $\mu = 0.0$ and their influence on the performance of the assembly.

As seen on the isolated propeller, increasing the advance ratio leads to a diminution of the propeller thrust and torque. Due to a balance malfunction, the experimental load measurements could not be presented. The numerical studies (Figure 11 from Ref. 19) highlighted a maximum propeller performances in hover. The performances are then minimal at $\mu = 0.05$. For all $\mu \geq 0.10$, the performances remain unchanged.

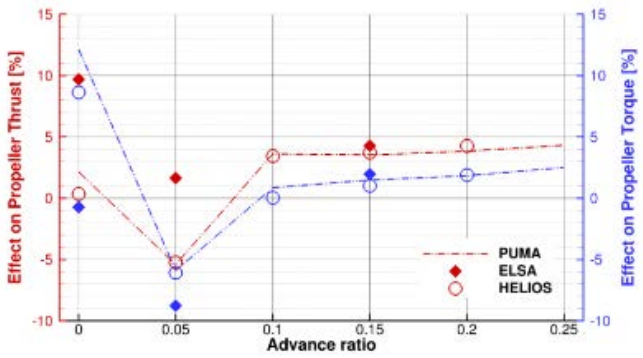

Figure 11 – Numerical estimation of thrust and torque of the mounted propeller for different advance ratios at Ωprop = 7632 rpm (Ref. 19)

In hover, numerical approaches (Ref. 20) predict that the rotor wake evolves at 14 m/s and impinges on the propeller at an angle of 90° (Figure 12). The preliminary studies carried out on the isolated propeller coupled with the numerical results thus put forward the positive influence of the interactions on the performances of the propeller in hover.

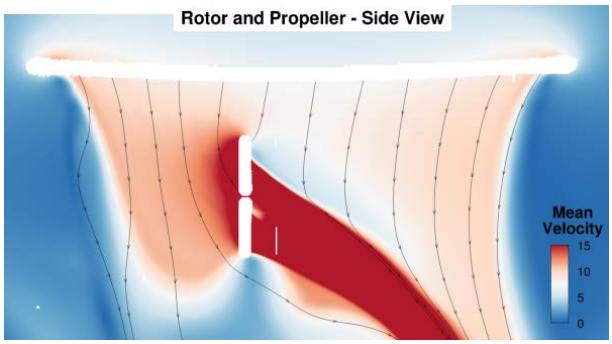

Figure 12 - Numerical estimation of the rotor wake development in hover (Ref. 21)

Knowing that the kettle is placed upstream to the honeycomb, only the activation of the wind tunnel could ensure an homogeneous seeding in the test section. Therefore, no velocity fields measurements could be conducted in hover.

This article will therefore explore experimentally the flow field around the structure for different advance ratios to validate the numerical approach.

Interactions at Low Speed

Efforts measurements showed that low speed flights present intermediate propeller performances. In this context, PIV measurements have been conducted to visualize the interactions between the rotating elements for this flight configuration. The influence of the rotor wake on the inlet conditions of the propeller is here examined to explain the efforts variations observed.

In the upper right corner of the plane of the Figure 13, an acceleration of the in-plane velocity is observed and is clearly due to the rotor wake. Therefore, the figure highlights that the propeller is partially immerged in the rotor wake. The norm of the velocity is increased within the wake, and reaches speeds up to 14 m/s. Whereas the flow is parallel to the $\vec{x}$ axis in the far field, it evolves at an angle of 44° in the rotor wake as highlighted by the streamlines. In the bottom right corner, an acceleration of the flow under the influence of the propeller suction is measured. The suction of the propeller also generates a decrease of the rotor wake angle up to 30° right upstream of the propeller disk.

As seen during the preliminary study on the isolated propeller, increasing the angle of attack maximizes the local thrust. Therefore, for this flight case, the rotor/propeller interactions lead to increased performances on the upper part of the propeller. However, the flow on the propeller is highly asymmetrical, which generates strong vibrations and in-plane loads not presented in the present paper. Overall, the inflow assymetry leads to decreased thrust and torque of the propeller for this flight configuration.

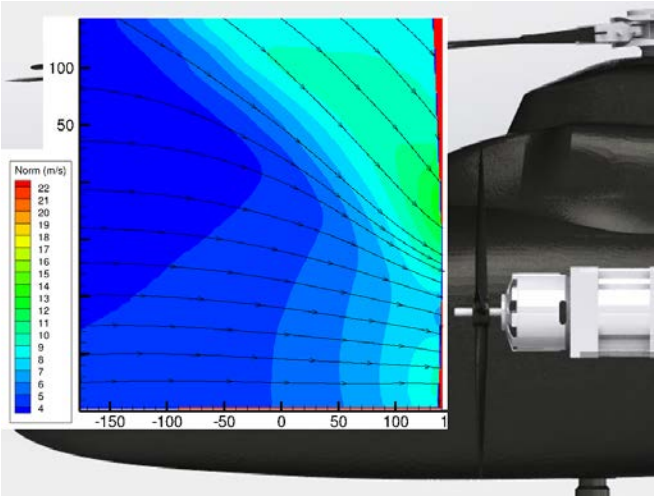

Figure 13 - In-plane velocity field at μ = 0.06

The rotor wake can also be identified by an increased value on the out of-plane velocity color map (Figure 14). $\vec{W}$ is negative inside the rotor wake, which is due to the influence of the rotating direction of the rotor on the flow. In the PIV plane placed under the advancing side of the rotor, this is transcribed by a passage of the blade from the front right to the back left.

The rotor wake boundary is also highlighted. Indeed, the upstream flow evolving at 5 m/s is confronted to the rotor wake whose norm is about 14 m/s. In parallel, the flow inside the wake is lead by the rotor blades and oriented towards the rotor center. Consequently a local winding of the free flow towards the exterior of the rotor disk is observed at the contact region due to the velocity gradient and the out of-plane component inside the rotor wake. This generates a strong out of-plane velocity under the wake boundary.

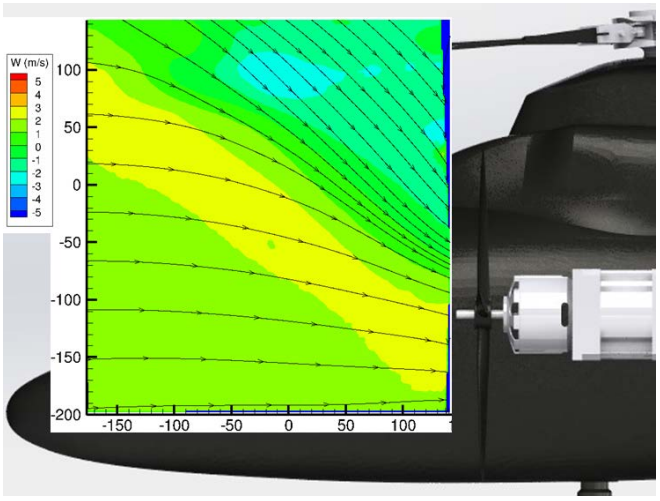

Figure 14 – Out of-plane velocity field at μ = 0.06

A vortex detection analysis has been conducted on the instantaneous images. The Γ2–criterion has been chosen has previous studies highlighted the reliability of this method for rotorcraft applications (Ref. 22). The authors identified the value of $2/\pi$ as a threshold to locate the vortex. Therefore only the points with $|\Gamma 2| > 2/\pi$ are plotted in Figure 15, showing one example of instantaneous vortex detection analysis. In this context, strong vortex regions are observed : 1) at the rotor wake boundary, as suggested by the averaged velocity fields images, and 2) under the rotor disk due to the passage of the blade tip vortices.

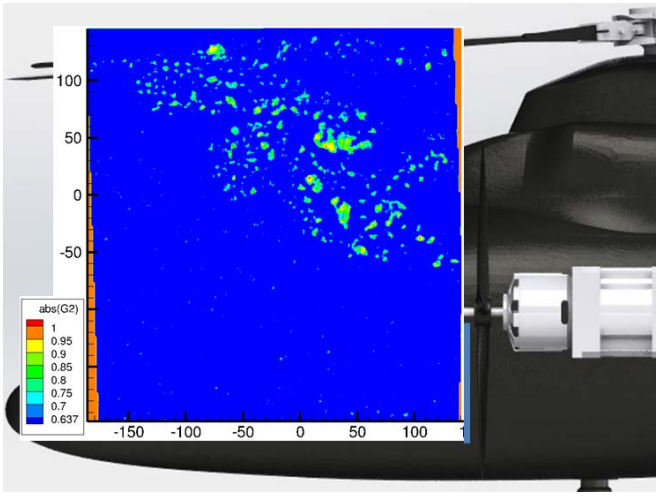

Figure 15 – Instantaneous vortex detection at μ = 0.06

The standard deviation of the velocities is less than 5 % in the undisturbed flow, but is more important for the zones undergoing important circulation. Peaks up to 20 % of the upstream flow are observed at the boundary of the rotor wake due to the strong turbulence.

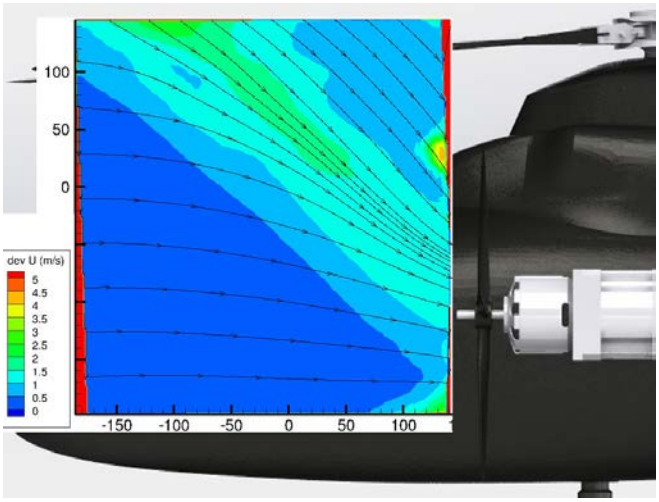

Figure 16 - Standard deviation of U at μ = 0.06

Interactions at High Speed

At high speed, the rotor wake passes well above the propeller and no direct rotor/propeller interactions are measured (Figure 17). Due to the limited influence of the rotor wake on the propeller, the propeller thrust is reduced compared to hover.

At μ = 0.22, an important out of plane velocity is observed on the upper side of the plane: this illustrates the intersection between the rotor wake and the upstream flow. Increasing the wind speed leads to a larger velocity gradient between the two flows, thus increasing the region of important out of-plane velocity. Once again it is supposed that the out of-plane velocity is caused by the influence of the rotation direction of the rotor blades sucking the flow towards the back of the plane.

As seen at μ = 0.06 the suction exerted by the propeller generates an increase of the velocity in the lower right corner (Figure 18). Increasing the advance ratio leads to a more important influence of the propeller: while the propeller suction is only measured 0.15 m upstream at μ = 0.06, the free flow on the entire PIV plane is affected at μ = 0.22. A velocity peak is also measured over the propeller blade tip, highlighting the acceleration of the flow inside the rotor wake.

The vortex detection analysis shows no strong values : only noise could be meausred with the available tools.

A small standard deviation is measured in the undisturbed flow. Standard deviations up to 20% are measured at the rotor wake boundaries (Figure 20). This figure also illustrates the suction of the flow by the rotor disk at high speed.

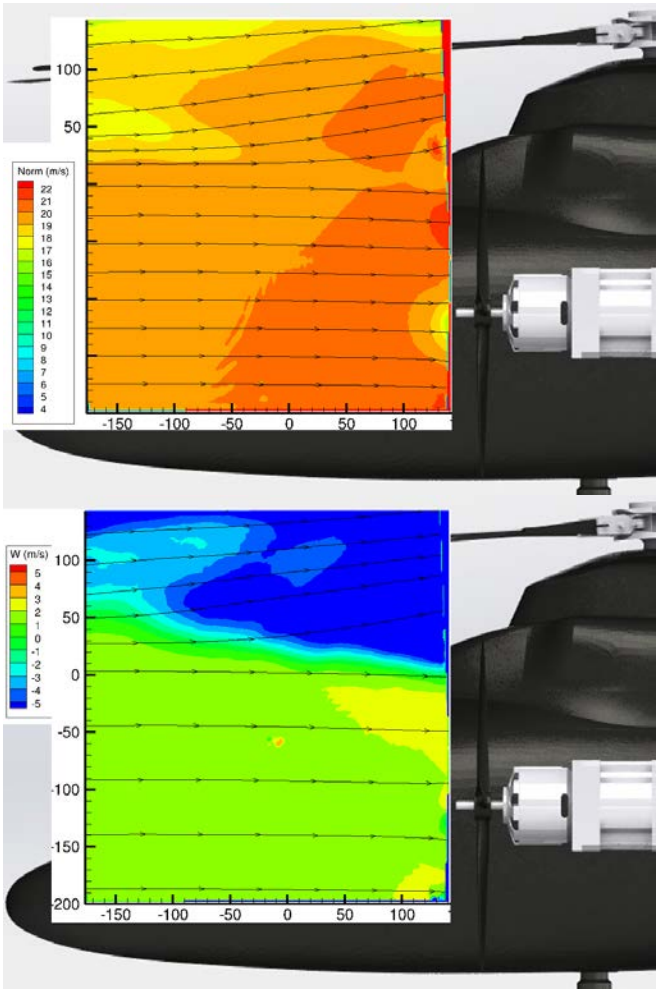

Figure 17 – In-plane norm (top) and out of-plane (bottom) velocity field at μ = 0.22

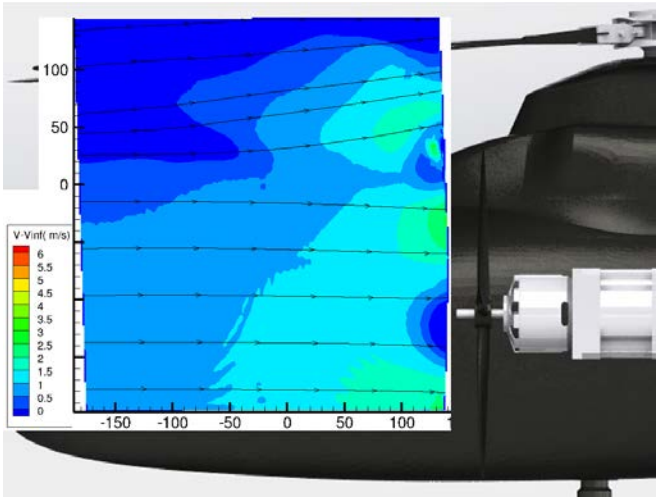

Figure 18 - In plane differential velocity at μ = 0.22

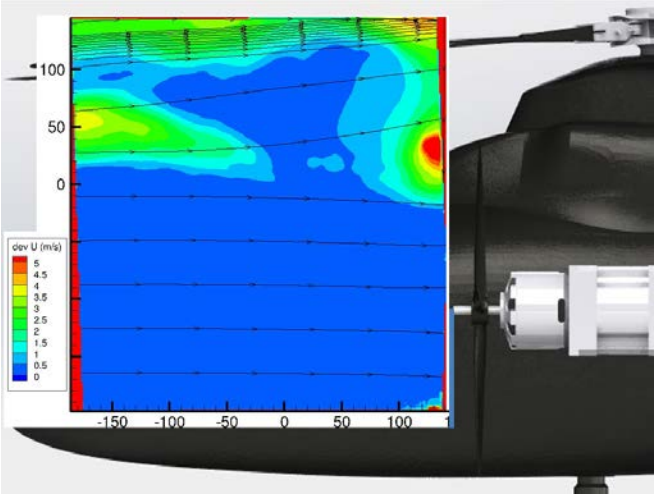

Figure 19 - Standard deviation of U at μ = 0.22

Influence of the Advance Ratio

The evolution of the angle and of the norm of the in-plane velocity under the influence of the rotating elements is presented in Figure 21. The flow angle is defined with $\alpha = \arctan(V/U)$, and is positive when the flow is tilted towards the ground. This analysis is conducted at x = 140 mm, just upstream of the propeller.

Increasing the advance ratio leads to a deceleration and a diminution of the flow angle on the upper part of the image. Indeed, at μ = 0.06, angles up to 50° are observed locally inside the rotor wake. A strong acceleration is observed inside the rotor wake: a peak is measured just under the propeller blade tip, where the flow is subject to the rotor wake and the propeller suction.

At μ = 0.12 the rotor wake is still present in the upper part of the image where a small acceleration and angles up to 25° are measured, but no influence on the propeller arise. A deceleration and realignment are then measured at the rotor wake boundary due to the interactions with the free flow.

At μ = 0.17 the rotor wake does not have a strong influence on the development of the flow as the angle remains small on the entire window. At μ = 0.22 a negative angle is observed in the upper part of the plane, highlighting the suction of the flow by the rotor. For all μ ≥ 0.17 a flow deceleration is measured on the upper part of the image, just under the rotor disk. This figure therefore highlights the absence of direct rotor/propeller interactions for all μ ≥ 0.12.

The lower part of the image underlines the similar propeller suction effect for all advance ratios in the close field. A velocity maximum is observed at around y = -25 mm, just under the propeller blade tip. An in-plane angle maximum is also measured at y = 0 mm. Velocity and angle peaks are observed at the center of the propeller disk (y = -130 mm) due to the sudden loss of local thrust.

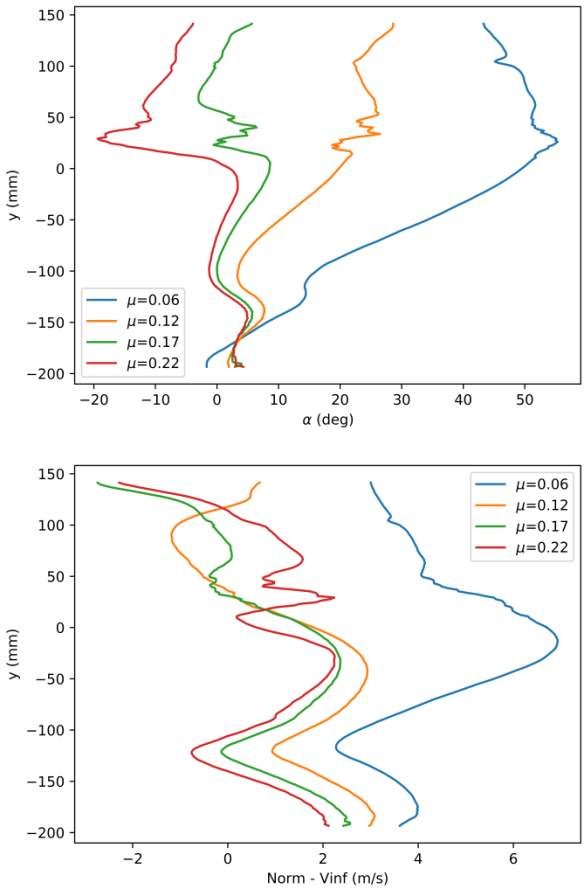

Figure 20 – Angle and norm of the flow for different advance ratio at x = 140 mm

CONCLUSIONS

The aim of this study was to identify the influence of the rotor/propeller interactions on the performance of the aircraft, and to validate the numerical approach.

Increasing the advance ratio leads to a decrease in propeller thurst due to the modification of the local angle of attack of the flow on the propeller blades. This phenomena is observable on the isolated propeller, and is increased by the interactions with the rotor wake.

Considering this, the influence of the interactions in hover were examined: the numerical studies predict that the thurst and the torque of the propeller are maximal at μ = 0.0. No experimental velocity field measurements could be performed, but the calculations highlighted that the wake impacts the propeller at 90° with a velocity of 14 m/s. This allows the propeller to ensure an efficient anti-torque and to increase the manoeuvrability of the helicopter.

A detailed analysis of the rotor wake development as a function of the advance ratio has been also carried out.

At $\mu = 0.06$, the effect of the free-flow and the rotor wake are combined. The angle of attack of the flow on the propeller disk is of 30° on the upper part of the propeller immersed in the rotor wake, and about 0° on the lower half which is only subjected to the upstream flow. In this flight case, the thrust is slightly decreased under the influence of the interactions.

Finally, at high speeds ($\mu \geq 0.12$), the rotor wake passes above the propeller and no direct interaction is observed.

High out of-plane regions have been identified at the rotor wake boundary, and just upstream to the propeller due to the suction exerted. Vortex regions appear under the rotor disk due to the rotor blade tip vortices, and at the rotor wake boundary.

Overall, the numerical and experimental approaches show similar velocity profiles for all the advance ratios. The differences are explained by 1) a slightly modified rotor dynamics, and 2) the different rotor rotational speed set under the experimental constraints.

Further tests will be done to enrich the experimental data base about rotor/propeller interactions. First and foremost, the loads measurements showed some surprising results. Complementary tests will therefore be conducted to verify the repetability of the measures and to investigate new flight configurations. On the other hand, this article only presents the interactions on the nominal configuration of the Eurocopter X3. It is therefore interesting to investigate the variations of loads and velocity fields for different propeller positions. Additional tests will also be conducted under the retreating side of the rotor to highlight the influence of the rotating direction of the off-plane velocity profile. Complementary PIV tests will also be conducted to measure the velocity fields just downstream of the propeller to examine the wake interactions and the development of the rotor wake towards the tail of the device.

Author contact: Lauriane Lefevre, lauriane.lefevre@onera.fr

ACKNOWLEDGMENTS

The authors gratefully acknowledge the financial support given by ONERA and the region Hauts-de-France. The technical support of Ronan Boisard and François Richez for the numerical study is also thanked.

REFERENCES

[1] M. Orchard and S. Newman, « The fundamental configuration and design of the compound helicopter », J. Aerosp. Eng., vol. 217, no 6, p. 297‑315, June 2003, doi: 10.1243/095441003772538570.

[2] M. Floros and W. Johnson, « Performance Analysis of the Slowed-Rotor Compound Helicopter Configuration », J. Am. Helicopter Soc., vol. 54, no 2, p. 22002, avr. 2009, doi: 10.4050/JAHS.54.022002.

[3] K. Ferguson and D. Thomson, « Flight dynamics investigation of compound helicopter configurations », J. Aircr., vol. 52, p. 156‑167, Jan. 2015.

[4] P. Lorber *et al.*, « Overview of S-97 RAIDER Scale Model Tests », in AHS International Forum 72, West Palm Beach, Florida, May 2016.

[5] C. Öhrle *et al.*, « Compound Helicopter X 3 in High-Speed Flight: Correlation of Simulation and Flight Test », J. Am. Helicopter Soc., vol. 66, no 1, p. 1‑14, Jan. 2021, doi: 10.4050/JAHS.66.012011.

[6] O. Rand and V. Khromov, « Compound Helicopter: Insight and Optimization », J. Am. Helicopter Soc., vol. 60, janv. 2015, doi: 10.4050/JAHS.60.012001.

[7] C. M. Russell and W. Johnson, « Conceptual Design and Performance Analysis for a Large Civil Compound Helicopter », in AHS Future Vertical Lift Aircraft Design Conference, San Francisco, CA, Jan. 2012.

[8] J. Thiemeier, C. Öhrle, F. Frey, M. Keßler, and E. Krämer, « Aerodynamics and flight mechanics analysis of Airbus Helicopters' compound helicopter RACER in hover under crosswind conditions », CEAS Aeronaut. J., Apr. 2019, doi: 10.1007/s13272-019-00392-3.

[9] H. Yeo and W. Johnson, « Aeromechanics Analysis of a Compound Helicopter », in American Helicopter Society 62nd Annual Forum, Phoenix, Az, May 2006.

[10] L. Lefevre, V. Nowinski, J. Delva, and A. Dazin, « Experimental Evaluation of the Aerodynamic Rotor/Propeller Interactions in Hybrid Compound Helicopters », in 47th European Rotorcraft Forum, sept. 2021.

[11] T. C. A. Stokkermans, « Aerodynamics of Propellers in Interaction Dominated Flowfields », PhD thesis, TU Delft, Delft, The Netherlands, 2020.

[12] Le Pape A., Gatard J., and Monnier J.-C., « Experimental Investigation of Rotor-Fuselage Aerodynamic Interactions », J. Am. Helicopter Soc., vol. 52, no 2, p. 99, Apr. 2007, doi: 10.4050/JAHS.52.99.

[13] T. Renaud, M. Smith, M. Potsdam, and D. O'Brien, « Evaluation of isolated fuselage and rotor-fuselage interaction using Computational Fluid Dynamics », J. Am. Helicopter Soc., vol. 53, no 1, p. 3‑17, Jan. 2008, doi: 10.4050/JAHS.53.3.

[14] L. Cambier and J.-P. Veuillot, « Status of the elsA Software for Flow Simulation and Multi-Disciplinary Applications », in 46th AIAA Aerospace Sciences Meeting and Exhibit, American Institute of Aeronautics and Astronautics. doi: 10.2514/6.2008-664.

[15] F. Champagnat, A. Plyer, G. Le Besnerais, B. Leclaire, S. Davoust, and Y. Le Sant, « Fast and accurate PIV computation using highly parallel iterative correlation maximization », Exp. Fluids, vol. 50, no 4, p. 1169, Mar. 2011, doi: 10.1007/s00348-011-1054-x.

[16] G. Le Besnerais and F. Champagnat, « Dense optical flow by iterative local window registration », in IEEE International Conference on Image Processing 2005, Sept. 2005, vol. 1, p. I‑137. doi: 10.1109/ICIP.2005.1529706.

[17] B. Benoit, A.-M. Dequin, K. Kampa, W. Grünhagen, P.-M. Basset, and B. Gimonet, « HOST, a General Helicopter Simulation Tool for Germany and France », Jan. 2000.

[18] L. Lefevre and V. Nowinski, « Characterization of the propeller for the experimental evaluation of the aerodynamic rotor/propeller interactions in hybrid compound helicopters », in Onera - DLR Aerospace Symposium, Braunschweig, Germany, Nov. 2020.

[19] R. Boisard and J. W. Lim, « Aerodynamic analysis of rotor/propeller wakes interactions on high speed compound helicopter », in 47th European Rotorcraft Forum, UK, Sept. 2021.

[20] R. Boisard, « Aerodynamic investigation of rotor/propeller interactions on a fast rotorcraft », Delft, The Netherlands, Sept. 2018, vol. 13, p. 14.

[21] R. Boisard, « Numerical Analysis of Rotor/Propeller Aerodynamic Interactions on a High-Speed Compound Helicopter », Vertical Flight Society, Oct. 2021. doi: 10.4050/JAHS.67.012005.

[22] F. De Gregorio and A. Visingardi, « Vortex detection criteria assessment for PIV data in rotorcraft applications », Exp. Fluids, vol. 61, no 8, p. 179, Aug. 2020, doi: 10.1007/s00348-020-03012-7.